

# Micromechanical analysis of the cyclic mechanical response of granular materials through DEM simulations

M. Victoria Molina<sup>1,\*</sup>, Roberto Cudmani<sup>1</sup>, and Andrés Alfonso Peña-Olarte<sup>2</sup>

<sup>1</sup>Center for Geotechnics, Technical University of Munich, 81245 Munich, Germany

<sup>2</sup>Civil Engineering Department, University of Applied Sciences Potsdam, 14469 Potsdam, Germany

**Abstract.** In this study, we investigate with the Discrete Element Method (DEM) the mechanical behavior of a cohesionless granular material under undrained true triaxial conditions, considering both monotonic and cyclic loading. We link the microstructure evolution within the granular assembly to its macroscopic cyclic response. To capture the mechanical response of our reference material (Karlsruhe fine sand), a rolling resistance linear contact model along with spherical particles is calibrated through a trial-and-error process, adjusting the model parameters to capture the experimentally observed behavior as close as possible. A series of cyclic undrained triaxial tests were simulated to investigate the micromechanical processes underlying liquefaction of sand under cyclic shearing. We analyzed the evolution of various fabric indices, including the redundancy index, contact normal orientations, and fabric anisotropy in relation to the pre- and post-liquefaction responses. The results reveal that a redundancy index below unity provides a unified criterion for the loss of the isostatic condition within the granular assembly, which triggers the onset of liquefaction. Throughout the cyclic loading process, sliding-dominant contact-yielding mechanisms remain prevalent. Additionally, significant changes in contact normal orientation and increasing fabric anisotropy dependent on the induced axial strain occur as the sample undergoes post-liquefaction deformation.

## 1 Introduction

Liquefaction is a natural phenomenon in saturated granular soils, characterized by a decrease in effective stress toward zero due to increased pore water pressure, and a reduction in shear strength or stiffness under undrained conditions. Liquefaction, static or triggered by cyclic loads, causes the soil's behavior to go from solid-like to liquid-like. Over the past decades, the geotechnical community has extensively studied liquefaction potential and triggering conditions through well-controlled laboratory tests and numerical analyses based primarily on a continuum approach. However, while macroscopic behavior is closely associated with microstructural evolution [1], these methods cannot provide particle-scale information to explore the fundamental mechanisms underlying macro-scale phenomena. The Discrete Element Method (DEM) enables the analysis of phenomena at the particle and mesoscale levels that govern the macro-mechanical response of the medium.

This study performs 3D DEM simulations on a cohesionless granular material. The contact model parameters were adjusted to capture the macroscopic response of Karlsruhe fine sand under monotonic triaxial loading. In a following stage, a series of DEM cyclic triaxial tests under undrained conditions using the constant-volume method are conducted on the specimens to explore the pre- and post-liquefaction behavior of sand through micromechanical signatures.

Key micromechanical variables examined include the redundancy index—which assesses system stability by accounting for sliding and rolling contacts—and the contact-normal-based fabric tensor, which reflects the orientation of inter-particle contacts.

## 2 DEM Model

DEM simulations were conducted using the open-source software YADE with a rolling resistance linear contact model for spherical particles to mimic grain shape and roughness. The model considers linear compression in the normal direction and in the tangential and rolling directions a linear response with limited strength to determine contact sliding and rolling. In the twisting direction, no plastic limit was applied; hence, the twisting moment accumulates elastically, and particles do not rotate freely in torsion.

The studied material is Karlsruhe fine sand—a typical quartz sand with sub-angular grains—using the experimental database compiled by Wichtmann and Triantafyllidis in [2]. DEM contact parameters were calibrated iteratively through monotonic drained and undrained triaxial test simulations until a fairly good agreement between the numerical response and the experimental results is reached. This calibration process is challenging because different parameter combinations can yield similar bulk responses, making it necessary to calibrate under different drainage and loading conditions [3]. The calibrated contact law parameters

\* Corresponding author: [victoria.molina@tum.de](mailto:victoria.molina@tum.de)

are as follows: a Contact stiffness of  $1e^{10}$  Pa, a contact stiffness ratio of 0.3, a Rolling stiffness of 0.3, a Rolling coefficient of 0.5, and an inter-particle friction angle of  $18^\circ$ . Since spherical particles cannot reproduce the initial void ratios obtained in the real sand samples, sample preparation in DEM targets the relative density  $D_r$  given as:

$$D_r = \frac{e_{max} - e}{e_{max} - e_{min}} \quad (1)$$

The limiting void ratios for Karlsruhe fine sand are  $e_{min}=0.677$  and  $e_{max}=1.054$ , determined from standard tests (DIN 18126[31]). In DEM,  $e_{min}$  is obtained by isotropic compression at a low confining pressure ( $p=10$  kPa) without interparticle friction,  $e_{max}$  is achieved through a pluviation process, obtaining limiting values of 0.568 and 0.841, respectively.

A cloud of 10,000 non-overlapping spherical particles was randomly generated in a  $10 \times 10 \times 10$  mm<sup>3</sup> cubic domain enclosed by frictionless rigid boundaries. Particle radii were assigned following Karlsruhe sand's (up-scaled) particle size distribution to avoid high computational times. Gravitational forces were neglected, and the contact friction angle was set to achieve different initial relative densities. The assembly was isotropically compressed using servo control mechanism until a initial confining pressure of  $p'_0=200$  kPa was reached.

To simulate undrained conditions in triaxial tests, the volume was kept constant by imposing a constant axial strain rate and half that rate in the lateral directions. A cyclic deviatoric stress amplitude ( $q_{amp}$ ) was imposed during the cyclic tests, with the loading being reversed upon reaching the prescribed amplitude in both compression and extension directions.

### 3 Simulations results

#### 3.1 Monotonic response

Simulation results from undrained triaxial compression and extension tests on samples with different initial relative densities and confining pressure of 200 kPa are compared with the lab experiments in Fig. 1. For the loose sample ( $D_r = 0.30$ ), both contractive and dilative tendencies are well reproduced. The slopes of the quasi-steady state (QSS) and steady state (SS) lines agree with experiments. However, the DEM model overestimates the deviatoric stress at the instability state (IS) (see Fig. 1(a)).

The results for medium-dense and dense samples ( $D_r = 0.64$  and  $D_r = 0.88$ , respectively) show a stiffer stress response at the beginning of shearing and a persistently dilative stress-strain response compared to experiments (see Fig. 1(a)). These discrepancies can be attributed to sample preparation techniques. As noted by Bernhardt et al. [4], the higher inter-particle friction angle used during shearing compared to one used during isotropic compression—aimed at achieving a denser packing—results in an increased frictional sliding limit, stabilizing contacts and reducing sliding at the beginning of shearing. Consequently, the simulations exhibit high stiffness and an early dilative response.

Additionally, Hanley et al. [5] reported that the constant-volume approach can produce unrealistically high deviatoric stresses when shearing dense samples, which is why authors might often report results in non-dimensional terms (e.g., stress ratios  $q/p'$ ).

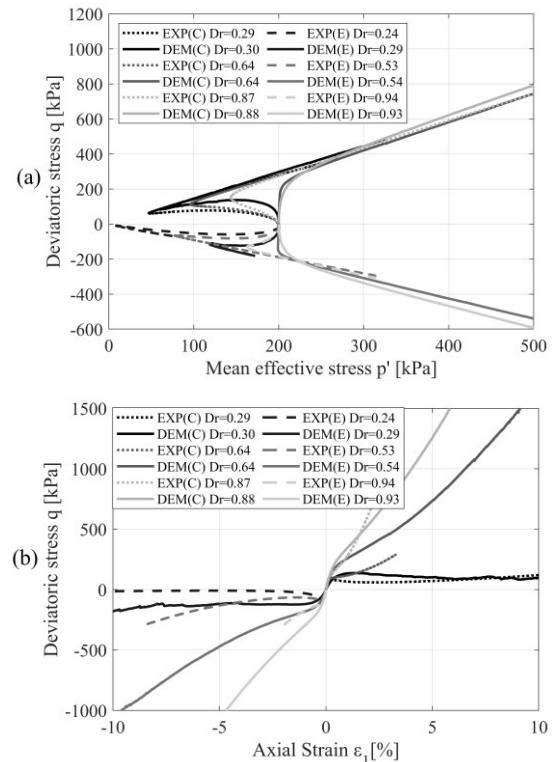


**Fig. 1.** Undrained monotonic triaxial tests: (a) effective stress path in the  $p'$ - $q$  plane, (b) stress-strain response

#### 3.2 Cyclic response

Strain-controlled undrained cyclic triaxial tests with ( $q_{amp}=60$  kPa) were performed on a medium-dense sample at an initial confining pressure of 200 kPa.

Fig. 2 compares the simulation stress-strain curves with experimental data. In the simulations, the onset of liquefaction is considered when the mean effective stress  $p'$  drops close to zero (i.e.,  $p'/p_0 < 0.01$ ). DEM results show a slower degradation rate of  $p'$  towards liquefaction, reaching liquefaction only after 17 cycles, compared to 11 cycles in the laboratory tests. At the onset of liquefaction, dilatancy causes  $p'$  to increase, but immediately after liquefaction at the reversal of loading the response switches from dilative to contractive upon reaching the specified  $q_{amp}$ . The model accurately reproduces the butterfly-shaped stress path in subsequent cycles, capturing the typical behavior of medium-dense sands (See Fig. 2(a)). While negligible axial strain accumulates during the pre-liquefaction stage ( $\epsilon_{1\_DEM} = 0.05\%$ ,  $\epsilon_{1\_EXP} = 0.17\%$ ), in the post-liquefied state—when the deviatoric stress is close to zero—axial strain accumulates in both compression and extension directions, with more pronounced strain in the extension direction, as observed in the experiment (See Fig. 2(b)).

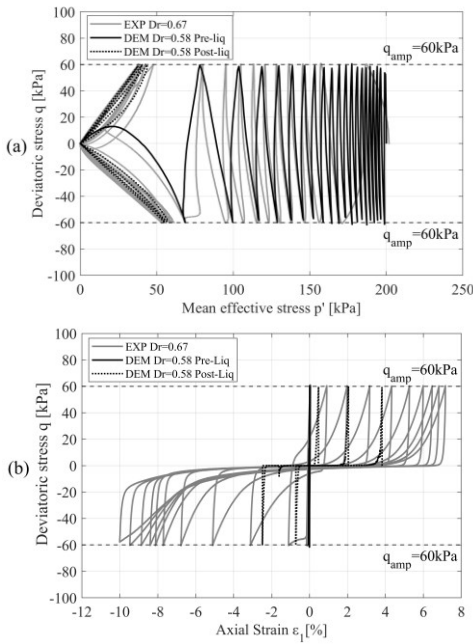


**Fig. 2.** Undrained cyclic triaxial test: (a) effective stress path in the  $p'$ - $q$  plane, (b) stress-strain response

#### 4 Micromechanical Analysis

A parameter for assessing mechanical stability is the redundancy index  $I_R$ , defined as the ratio of the total number of constraints to the total number of degrees of freedom (six in 3D) of the active particles [6].  $I_R$  is computed based on the constraint forces at particle contacts: normal force, two components of tangential force, two components of the rolling moment and twisting moment. Since the contact model considers only two yielding contact mechanisms—sliding and rolling—twisting is excluded from  $I_R$  calculation as:

$$I_R = \frac{6C_{NSR} + 4C_S + 4C_R + 2C_{SR}}{6(N - N_0)} \quad (2)$$

$C_{NSR}$  represents contacts that are neither sliding nor rolling,  $C_S$  those that are sliding,  $C_R$  those rolling, and  $C_{SR}$  those simultaneously sliding and rolling.  $N$  is the total number of particles and  $N_0$  represents the particles without contacts, which do not contribute to force transmission and are therefore excluded from the calculation. From a structural mechanics perspective,  $I_R=1$  (the number of constraints equals the degrees of freedom) identifies isostatic conditions. Values above 1 indicate a hyperstatic, stable system, whereas values below 1 reflect a hypostatic, unstable configuration.

Fig. 3 (a) depicts the evolution of  $I_R$  alongside the normalized mean effective stress  $p'/p_0$  during cyclic shearing. Initially,  $I_R$  exceeds unity, indicating a stable system, and varies cyclically with an overall decreasing trend during the pre-liquefaction phase. Liquefaction onset—defined by  $p'/p_0 < 0.01$ —corresponds to a sudden drop of  $I_R$  below 1, marking the transition to packing instability. Zhan et al. [7] suggested  $I_R=1$  as a threshold for initial liquefaction; however, it might be inappropriate to refer to the transition from a liquid to a solid-like state in the cyclic mobility stage. When  $p'/p_0$  becomes again larger than 0.01,  $I_R$  is around 1.3, which is a suitable indicator of a re-established and stable

contact network. In the post-liquefaction stage, each loading direction reversal causes a drop in  $I_R$  to a local minimum value near 0.35, aligning with Martin et al. [8], who identified  $I_R=0.35$  as an indicator of full liquefaction.

Fig. 3 (b) shows the evolution of contact fractions during cyclic shearing. Overall, sliding and sliding-rolling contacts dominate over pure rolling, indicating that sliding is the primary yielding mechanism. Prior to liquefaction, the sliding contact fraction exhibits larger oscillations while the rolling fraction remains very low, suggesting stronger inhibited rotation. Post-liquefaction, the increased instability allows free rotation and the number of rolling contacts rises, remaining much lower than the sliding contacts though. In the post-liquefaction phase, immediately after a loading reversal, all contact fractions strongly oscillate. Subsequently, the sliding contact fraction increases and peaks when the specimen begins to transit back to a solid-like state ( $p'/p_0 > 0.01$ ), moment after which it decreases sharply, indicating a reformation of the contact network before the next transition to liquid-like state.

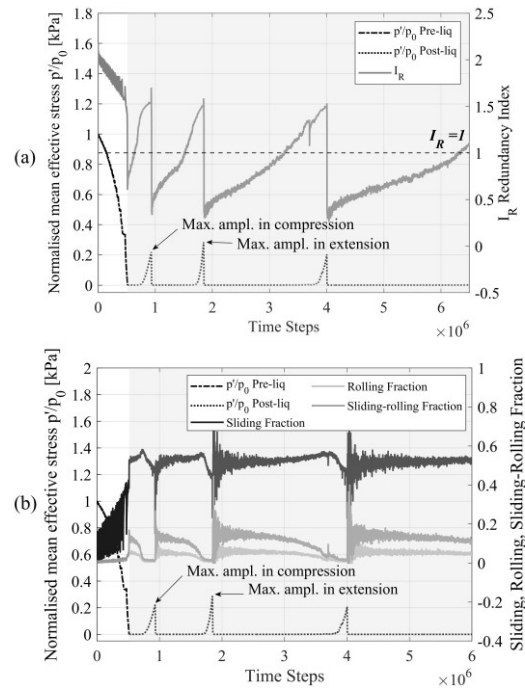


**Fig. 3.** Evolutions of (a) redundancy index and (b) contact fractions during cyclic triaxial test simulations

In micromechanics, ‘fabric’ describes the spatial distribution of micro-geometrical quantities, such as the orientation of contact normals, long axis of particles and voids, and branch vectors. Satake [9] first introduced the contact normal fabric tensor  $\mathbf{F}$  as a second-order tensor:

$$\mathbf{F} = \frac{1}{N_c} \sum_{k=1}^{N_c} \mathbf{n}_i^k \mathbf{n}_j^k \quad (3)$$

where  $\mathbf{n}_i^k$  and  $\mathbf{n}_j^k$  are the unit normal vectors of the  $k^{\text{th}}$  inter-particle contact, and  $N_c$  is the number of contacts.

The principal values of  $\mathbf{F}$  quantify the contact density along each principal stress direction, and the difference between the major and minor principal values has been used to define the intensity of contact normal fabric anisotropy of granular assemblies. Because non-diagonal terms are negligible in the presented true

triaxial simulations, the fabric anisotropy intensity can be defined as [7]:

$$F_{[y-x]} = F_{yy} - F_{xx} \quad (4)$$

$$F_{[y-z]} = F_{yy} - F_{zz} \quad (5)$$

Where  $F_{yy}$ ,  $F_{xx}$ , and  $F_{zz}$  are the normal components along the  $y$  (vertical),  $x$  and  $z$  (horizontal) directions.

Fig. 4 (a) shows the evolution of the three normal components of  $F$ .  $F_{xx}$  and  $F_{zz}$  evolve similarly under initial isotropic conditions and axisymmetric loading. After the onset of liquefaction,  $F_{yy}$  peaks during compression, and  $F_{xx}$  and  $F_{zz}$  experience minimum values. This is reversed in the next loading cycle towards extension, as contacts align with the applied stress direction to withstand external loads.

The evolutions of fabric anisotropy intensities are depicted in Fig. 4 (b). Prior to liquefaction, the anisotropy evolves cyclically with increasing amplitude; after liquefaction, low effective stresses facilitate the breaking and reorientation of contacts, resulting in higher anisotropy than in the pre-liquefaction stage. Upon load reversal, when  $I_R$  drops suddenly, anisotropy changes sign reflecting a collapse of existing force network and rapid reorientation of contact normal. As  $I_R$  increases ( $p'/p_0 > 0.01$ ), marking a reformation of contact network, anisotropy tends to decrease, indicating less directional bias and more uniform distribution of contacts. In subsequent cycles, fabric anisotropy continue to grow in amplitude with following cycles, indicating that the developed fabric anisotropy depends on the induced axial strain within a loading cycle.

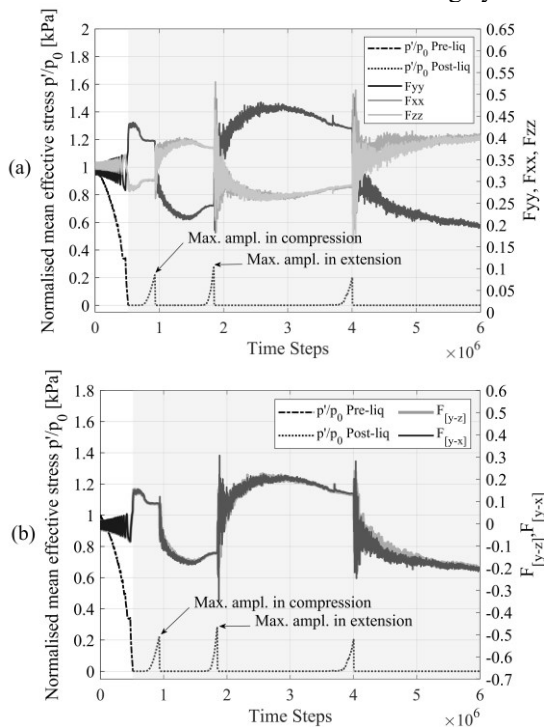


**Fig. 4.** Evolutions of (a) principal structural fabrics and (b) fabric anisotropy intensities during cyclic triaxial test simulations.

## 5 Conclusions

The DEM model incorporating spherical particles with rolling resistance captures the effect of irregular grain

shape under both monotonic and cyclic undrained triaxial loading. Although the DEM model reasonably approximates Karlsruhe fine sand behavior, it has limitations in quantitatively reproducing the initial shearing response (stiffness) during monotonic tests for dense samples—likely due to sample preparation techniques and the constant-volume method used to simulate undrained conditions. Key micromechanical findings include:

The onset of liquefaction is associated with the system becoming isostatic ( $I_R < 1$ ). Post-liquefaction,  $I_R$  reaches a minimum value of 0.35 and increases above 1 for a new loading cycle. Sliding dominates the contact-yielding mechanism throughout cyclic loading. As the specimen transitions from a liquid-like to a solid-like state, the fraction of sliding contacts peaks and then decreases. High redundancy corresponds to a more uniform contact structure, while strong anisotropy is more prominent during transient stages where contact realignment dominates the response. The evolution of the contact normal fabric shows that anisotropy intensifies with cyclic loading—especially after liquefaction—and depends on the induced axial strain.

## References

1. M.D. Bolton, The role of micro-mechanics in soil mechanics, in Proc. Int. Workshop on Soil Crushability, Yamaguchi Univ., Japan, also in CUED/D-Soils/TR313 (2000).
2. T. Wichtmann, Th. Triantafyllidis, An experimental database for the development, calibration and verification of constitutive models for sand with focus to cyclic loading. Part I: tests with monotonic loading and stress cycles, Acta Geotech. **11**(4), 739–761 (2016).
3. C.J. Coetzee, Review: Calibration of the discrete element method, Powder Technol. **310**, (2017).
4. M.L. Bernhardt, G. Biscontin, C. O’Sullivan, Experimental validation study of 3D direct simple shear DEM simulations, Soils Found. **56**(3), 336–347 (2016).
5. K.J. Hanley, X. Huang, C. O’Sullivan, F. Kwok, Challenges of simulating undrained tests using the constant volume method in DEM, AIP Conf. Proc. **1542**, 277–280 (2013).
6. G.B. Gong, C. Thornton, A.H.C. Chan, DEM simulations of undrained triaxial behavior of granular material, J. Eng. Mech. **138**(6), 560–566 (2012).
7. A. Zhang, M. Jiang, D. Wang, Effect of fabric anisotropy on the cyclic liquefaction of sands: Insight from DEM simulations, Comput. Geotech. **155**, 105188 (2023).
8. E.L. Martin, C. Thornton, S. Utili, Micromechanical investigation of liquefaction of granular media by cyclic 3D DEM tests, Géotechnique, 1–10 (2019).
9. M. Satake, Fabric tensor in granular materials, in Proc. IUTAM Symp. on Deformation and Failure of Granular Materials, Amsterdam, 63–68 (1982).